ACS APPLIED MATERIALS & INTERFACES

Research Article

www.acsami.org

Fast Responding Exhaled-Breath Sensors Using WO_3 Hemitubes Functionalized by Graphene-Based Electronic Sensitizers for Diagnosis of Diseases

Seon-Jin Choi,[†] Franz Fuchs,[‡] Renaud Demadrille,[‡] Benjamin Grévin,[‡] Bong-Hoon Jang,[†] Seo-Jin Lee,[†] Jong-Heun Lee,[§] Harry L. Tuller,[⊥] and Il-Doo Kim*[,†]

[†]Department of Materials Science and Engineering, Korea Advanced Institute of Science and Technology, 291 Daehak-ro, Yuseong-gu, Daejeon 305-701, Republic of Korea

[‡]SPrAM INAC UMR5819 (CEA-CNRS-UJF), CEA-GRENOBLE 17 rue des martyrs, F-38054 Grenoble Cedex 9, France

[§]Department of Materials Science and Engineering, Korea University, Anam-Dong, Seongbuk-Gu, Seoul 136-713, Republic of Korea

[⊥]Department of Materials Science and Engineering, Massachusettes Institute of Technology, Cambridge, Massachusetts 02139, United States

Supporting Information

ABSTRACT: Diagnostic sensing device using exhaled breath of human have critical advantages due to the noninvasive diagnosis and high potential for portable device with simple analysis process. Here, we report ultrafast as well as highly sensitive bumpy WO_3 hemitube nanostructure assisted by O_2 plasma surface modification with functionalization of graphene-based material for the detection of acetone (CH_3COCH_3) and hydrogen sulfide (H_2S) which are biomarkers for the diagnosis of diabetes and halitosis, respectively. 0.1 wt % graphene oxide (GO)- and 0.1 wt % thin layered graphite (GR)- WO_3 hemitube composites showed response times of 11.5 ± 2.5 s and 13.5 ± 3.4 s to 1 ppm acetone as well as 12.5 ± 1.9 s and 10.0 ± 1.6 s to 1 ppm of H_2S, respectively. In addition, low limits of detection (LOD) of 100 ppb (R_{air}/R_{gas} = 1.7 for acetone and R_{air}/R_{gas} = 3.3 for H_2S at 300 °C) were achieved. The superior sensing properties were ascribed to the electronic sensitization of graphene based materials by modulating space charged layers at the interfaces between n-type WO_3 hemitubes and p-type graphene based materials, as identified by Kelvin Probe Force Microscopy (KPFM). Rapid response and superior sensitivity of the proposed sensing materials following cyclic thermal aging demonstrates good potential for real-time exhaled breath diagnosis of diseases.

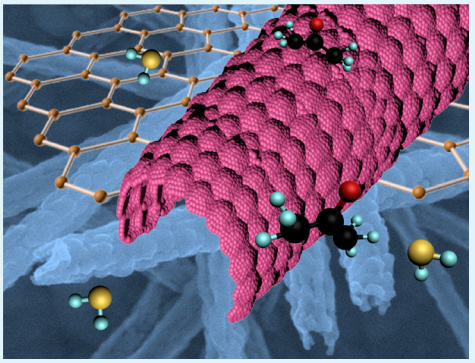

KEYWORDS: *diagnosis of diseases, exhaled breath sensor, electrospinning, WO_3 hemitube, graphene*

INTRODUCTION

Human breath contains a number of volatile organic compounds (VOCs). An accurate detection of specific VOCs in exhaled breath, known as biomarkers, can provide essential information for the diagnosis of those diseases. For example, acetone (CH_3COCH_3), H_2S, NH_3, NO, and toluene ($C_6H_5CH_3$) can be used to evaluate diabetes,[1,2] halitosis,[3] kidney malfunction,[4] asthma,[5] and lung cancer,[6] respectively. The diagnosis of these diseases can be achieved by analyzing exhaled breath gases originating from the molecular exchange between the lung tissue and blood. The noninvasive diagnosis of various diseases is the key advantage of exhaled breath analysis techniques over more commonly used methods such as a computed tomography or endoscope. As a consequence, gas chromatography/mass spectroscopy (GC/MS),[7,8] optical spectroscopy[9] and ion mobility spectrometry (IMS),[10] have been adopted to detect sub-parts per millions concentrations of VOCs in exhaled breath. However, these techniques are limited in terms of real time diagnosis, particularly relevant in this field, because of their bulky size and often complex and relatively slow measuring procedures.

To overcome these limitations, exhaled breath sensors, utilizing semiconducting metal oxides as the sensing elements, have begun to attract attention because of their simple operating principle (resistivity change upon exposure of various VOCs to the metal oxide surface layers), simple device fabrication, and ready miniaturization.[11] Several recent studies have demonstrated the feasibility of high performance VOC sensors using metal oxide nanostructures such as Fe_2O_3 hollow spheres,[12] Zn_2SnO_4 nanofibers,[13] and Co_3O_4 nanorods,[14] as well as WO_3 nanostructures.[15−17] In addition, surface treatment and modification methods including oxygen plasma etching[18] and phase separation assisted electrospinning[13,19] have been proposed for the synthesis of highly porous nanostructures,

Received: January 13, 2014
Accepted: May 20, 2014
Published: May 20, 2014

   dx.doi.org/10.1021/am501394r | ACS Appl. Mater. Interfaces 2014, 6, 9061−9070

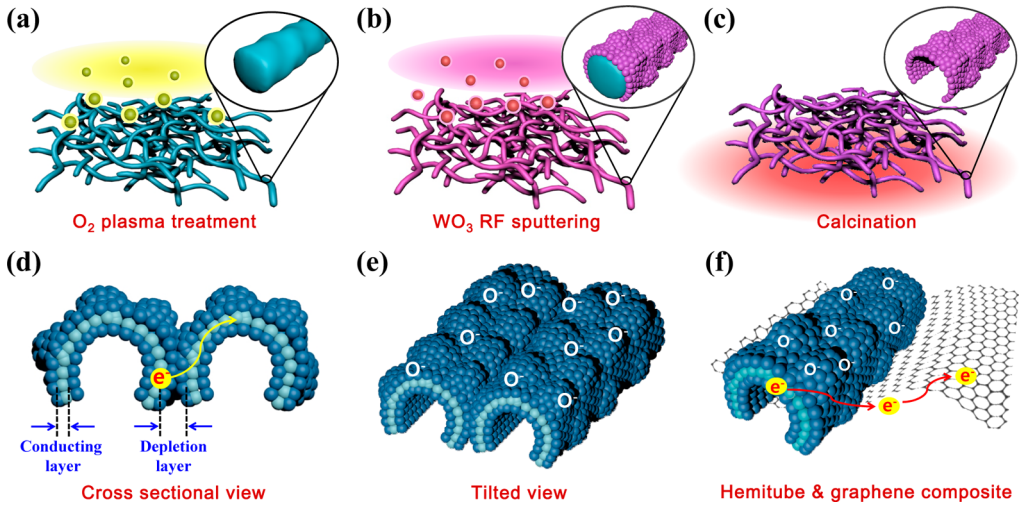

Figure 1. Schematic illustration of fabrication process: (a) surface modification of electrospun polymeric fiber template by O_2 plasma treatment, (b) WO_3 coating using RF sputtering, and (c) high-temperature calcination by decomposing the inner polymeric fiber template. (d, e) Homojunction between pristine WO_3 hemitubes and (f) a heterojunction between a graphene-based material and a WO_3 hemitube.

resulting in high sensitivity to VOCs. The highly porous nanostructures, in addition to providing large enhancements in the number of surface reaction sites, support modulation of the electron density across the full volume of the oxide particles rather than just a narrow depletion layer, given their nanosized cross sections. However, a key barrier to practical implementation of real-time breath sensors remains their relatively slow response and sluggish recovery times.[1,20] To enhance gas sensor response, as well as response/recovery kinetics, not only noble metal catalysts such as Pt,[21] Rh,[22] Ag,[23] Pd[24] but also semiconductor dopants such as Si[25,26] have been introduced to functionalize the surfaces of nanostructured metal oxides. More recently, composites composed of graphene-based materials[27,28] and metal oxides have been suggested as an alternative means for functionalizing chemical sensors.[29,30] Graphene is known to be capable of detecting single gas molecules, as well as possessing high electrical conductivity, thereby potentially providing superior sensitivity and more rapid response times.[31−35] Reduced graphene oxide (rGO)-WO_3 nanoparticles,[33] graphene-SnO_2 nanorods,[34] and graphene oxide (GO)-ZnO nanoparticles,[35] for example, have been demonstrated to detect NO_2, H_2S, and NH_3, respectively, in a dry air atmosphere. However, to the best of our knowledge, the application of composites based on graphene and thin-walled metal oxide tubes for VOC detection, in the context of exhaled breath analysis, have yet to be investigated, particularly under the high humidity conditions (85−95% RH) representative of human breath.

In this work, we report on a new VOC sensing material consisting of surface-modified WO_3 hemitube-graphene-based composites, utilizing for the latter, either thin graphite (GR) or graphene oxide (GO) layers. Exhaled breath sensors using composites of either GR- or GO-modified WO_3 hemitubes, demonstrate rapid response times and high gas sensitivity in humid atmosphere. Various preparation characterization and measurement techniques are examined with the objective of identifying morphologies and compositions for optimum performance. Kelvin probe force microscopy measurements are examined to further aid in understanding performance.

EXPERIMENTAL SECTION

Fabrication of WO_3 Hemitubes with Bumpy Surface. To achieve a rough, high surface area for metal oxide sensing materials and thereby stronger gas response, we coated oxygen plasma exposed polymer templates with WO_3 using PVD. For the polymer template, 0.5 g of polyvinylpyrollidone (PVP, M_w = 1 300 000 g mol^{-1}) and 0.5 g of poly(methyl methacrylate) (PMMA, M_w = 350 000 g mol^{-1}) were dissolved in 7.5 g of *N,N*-dimethylformamide (DMF) to form highly random fiber networks by electrospinning. The PVP/PMMA composite fibers were electropsun by applying 23 kV using a DC power supply with a distance of 17 cm between the tip of a stainless steel needle (21 gauge) and a ground plate. The electrospun PVP/PMMA composite fibers were introduced in a plasma chamber with a pressure of 9 Pa. Then, oxygen gas was injected into the chamber with a flow rate of 100 mL/min and stabilized for 30 s. RF power of 20 W was applied to generate the plasma and the treatment time lay in the range of 1−6 min (see Figure S1a−f in the Supporting Information). WO_3 films were deposited by RF sputtering with a 3 in. WO_3 target. After the base pressure reached 5 × 10^{-6} Torr, an Ar atmosphere with a working pressure of 1.0 × 10^{-2} Torr was achieved. During deposition, the RF power was maintained at 80 W and the deposition temperature was kept at room temperature to prevent the decomposition of the polymer nanofibers. The deposition rate was 6 nm/min as calibrated on a flat Si substrate. Deposition proceeded for 20 min on the plasma treated polymer nanofibers while rotating the substrate for uniform deposition. A post heat treatment was performed at 500 °C for 1 h in air with heating and cooling rates of 4 °C min^{-1} to vaporize the inner polymer nanofibers and thus to form the hollow bumpy WO_3 hemitubes.

Preparation of Thin Graphite (GR) and Graphene Oxide (GO) Layers. Graphite was prepared by dispersing with sonication of commercialized graphene flakes (Unithink Inc.) in *N,N*-dimethylformamide (DMF). More than 10 layers were stacked together in the preparation of the graphene flakes. Graphene oxide (GO) was obtained by exfoliating graphite by hummer's method[36] and dispersing it in DI water. The exfoliated GO exhibited, on average, 9−10 layers.

nc-AFM and KPFM Analysis of Bumpy WO_3 Hemitubes on HOPG. The WO_3 hemitubes were dissolved in ethanol and dropcast onto freshly cleaved HOPG (Highly Ordered Pyrolytic Graphite) substrates. The functionalized samples were subsequently introduced in an Omicron VT-AFM system at ultra high vacuum conditions (pressure ~5 × 10^{-11} mbar) and room temperature for noncontact atomic force microscopy (nc-AFM) investigations. After introduction the WO_3 samples were outgassed in vacuum for 1 h at 145 °C to remove remaining solvent. Also the bare HOPG reference sample was outgassed in vacuum in order to remove absorbates and to ensure a

dx.doi.org/10.1021/am501394r | ACS Appl. Mater. Interfaces 2014, 6, 9061−9070

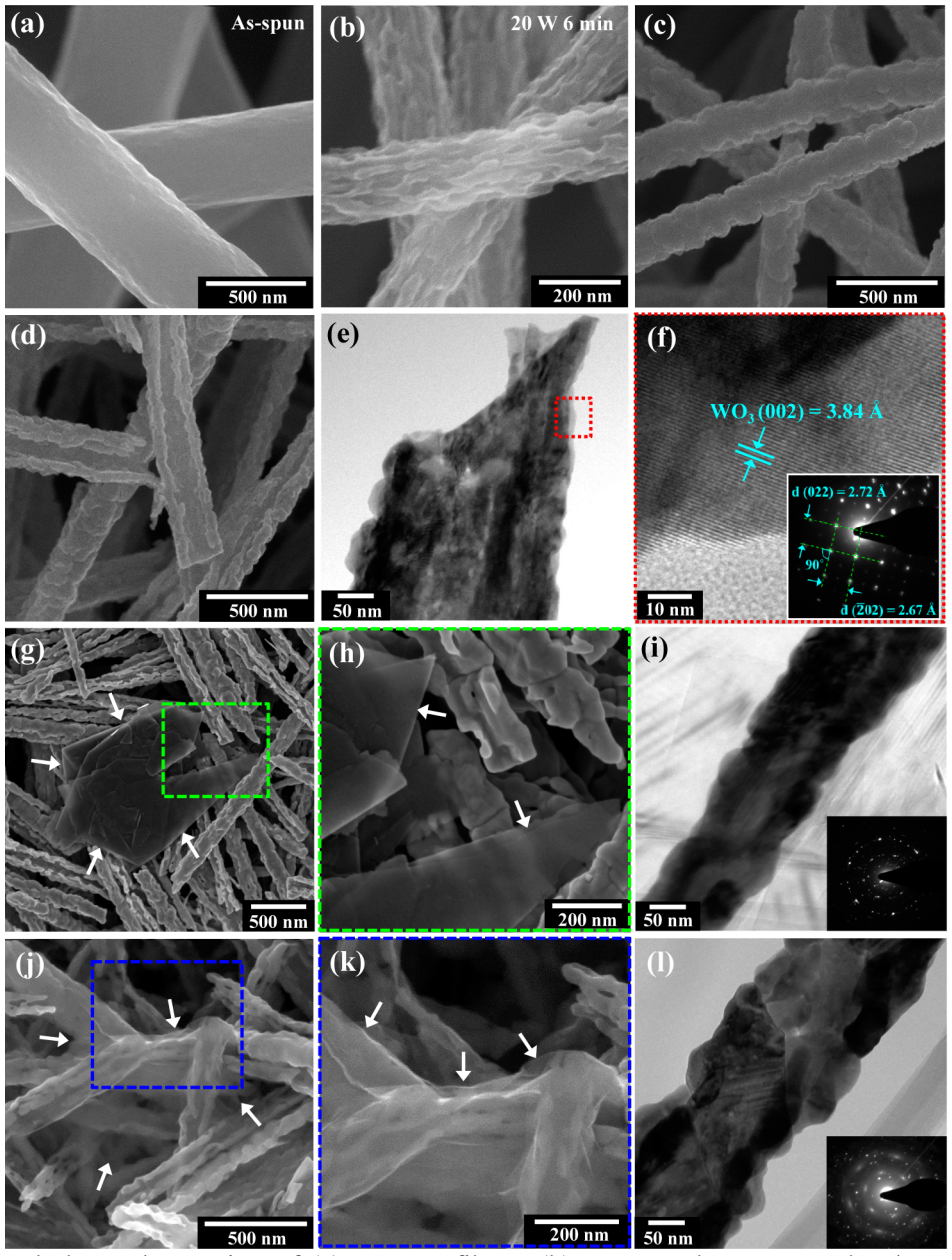

Figure 2. Morphology observation of (a) as-spun fibers, (b) oxygen plasma treated polymer fibers with fixed power of 20 W for 6 min, (c) WO_3 coated oxygen plasma-treated polymer fibers, (d) bumpy WO_3 hemitubes after calcination at 500 °C for 1 h, (e) TEM observation of the edge of bumpy WO_3 hemitube, (f) high-resolution (HR) TEM image and selected area electron diffraction (SAED) pattern of the crystallized WO_3 hemitubes in the inset. (g) SEM image of GR-WO_3 hemitube composite, (h) magnified image of g, (i) TEM image of GR-WO_3 composite with SAED pattern in the inset, (j) SEM image of GO-WO_3 hemitube composite, (k) magnified image of j, (l) TEM image of GO-WO_3 composite with SAED pattern in the inset.

well-defined work function. All nc-AFM and KPFM results were acquired with Pt–Ir coated cantilever (Nanosensors, PPP-EFM) with a resonance frequency of about 70 kHz and a quality factor on the order of 40 000. Prior to utilization the cantilever were equally outgassed to remove a possible water layer or contaminants. The KPFM measurements were performed in the amplitude modulation KPFM mode.[37]

Gas Sensor Characterization. VOC sensing properties were characterized using a homemade sensor test system (see Figure S2a in the Supporting Information). Several types of gases, H_2S, acetone, ethanol, NH_3, NO, pentane and CO, were tested in the concentration range of 1–5 ppm and the temperature range of 200–350 °C and in very high humid atmosphere (85–95% RH). Before measurements were begun, all sensors were stabilized for about 6 h in air to obtain a stable base resistance at each temperature. Each measurement cycle included 10 min target gas injection followed by 10 min air. Resistance changes were measured using a data acquisition system (34972A, Agilent) with a 16 channel multiplexer (34902A, Agilent). Temperature control was achieved by applying a controlled voltage from a DC power supply (E3647A, Agilent). All sensor specimens were coated on Al_2O_3 substrates whose front sides were patterned with parallel Au electrodes (see Figure S2b in the Supporting Information). A heater was located on the substrate backside to control sensor temperature (Figure S2c in the Supporting Information). The WO_3 hemitubes were coated on the front side of the Al_2O_3 substrate (see Figure S 2d in the Supporting Information). To investigate the thermal stability of the sensors, we performed cyclic tests from 200 to 350 °C with 4 repetitions.

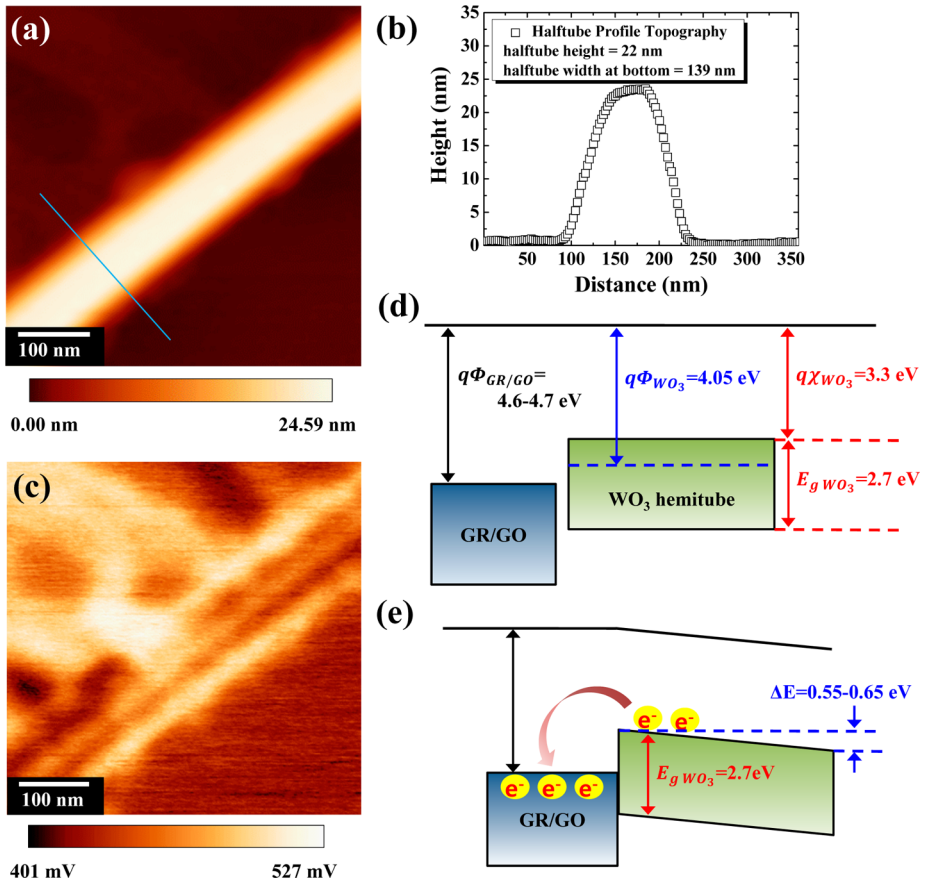

Figure 3. (a) Topographic nc-AFM image of a single WO_3 hemitube ($\Delta f = -5$ Hz, $f_{cantilever} = 71$ kHz, $A_{cantilever} = 24$ nm); (b) profile across WO_3 hemitube in topographic image (a) (profile location marked by blue line in a), typical values of 22 nm height and 139 nm width at bottom are obtained for the WO_3 hemitube; (c) contact potential difference image acquired simultaneously to the topographic image in (a) on the same sample area ($\Delta f = -5$ Hz, $f_{cantilever} = 71$ kHz, $A_{cantilever} = 24$ nm); (d) band structure model for GR/GO and WO_3 hemitubes relative to the vacuum level, the work function of WO_3 hemitubes has been determined by KPFM on a high coverage sample of WO_3 hemitubes on HOPG; (e) upon contact of the WO_3 hemitubes with GR/GO electron charge transfer happens from the hemitubes to the GR/GO, which causes band bending in the WO_3 of ΔE = 0.55 to 0.65 eV.

RESULTS AND DISCUSSION

Figure 1 shows the schematic illustration on fabrication process of very high surface area WO_3 hemitubes, as well as charge transport at WO_3 hemitubes homocontacts and between graphene and WO_3 hemitube heterocontacts. High-surface-area WO_3 hemitubes without (Figure 1d, e) and with functionalization by graphene layers (Figure 1f) were synthesized by first forming a nonwoven polymeric fiber template network, synthesized by electrospinning a poly-vinylpyrollidone (PVP)/poly(methyl methacrylate) (PMMA) composite. Hollow WO_3 hemitube structures were then achieved by RF-sputtering WO_3 films onto the electrospun PVP/PMMA composite nanofiber templates, followed by high temperature calcination.[20,38] To further increase the surface area of the WO_3 hemitubes, the surfaces of the polymeric fiber template were modified by an O_2 plasma treatment (Figure 1a), thereby providing a wrinkled, bumpy surface topology (Figure 1d, e). The microstructural changes were examined by high resolution microscopy (see below) and optimized by controlling the duration of the O_2 plasma treatment with a fixed RF power of 20 W. RF-sputtered WO_3 films covered the contours of the O_2 plasma-treated wrinkled template fibers (Figure 1b), leading to hollow, bumpy WO_3 hemitubes following calcination at 500 °C which served to decompose the supporting polymeric template (Figure 1c). Finally, graphene based materials were functionalized onto the WO_3 hemitubes by homogeneous mixing of the materials. As shown in Figure 1d and e, charge transport via homocontacts between adjacent WO_3 tubes is suppressed due to the formation of electron depletion layers, generated by electron localization at the O^- adions on the WO_3 hemitube surface. Charge injection at the hetro-interface between WO_3 hemitube and graphene is significantly enhanced relative to that of the homocontact (Figure 1f), leading to more rapid response times, given corresponding reductions in the RC time constants of the WO_3-graphene composite system.

Figure 2 shows the microstructural evolution and morphologies of the high surface area WO_3 hemitubes both single phase and those functionalized by thin graphite and graphene oxide sheets. As the O_2 plasma exposure time increased, the surface of as-spun PVP/PMMA fibers, with diameters in the range of 200−300 nm, became rougher and more crenelated compared to the initial smooth pristine fibers (Figure 2a, b). This wrinkled surface morphology likely resulted from the anisotropic attack of the polymeric fibers by the reactive oxygen to form H_2O and CO_2.[39] During the O_2 plasma treatment, a noticeable shrinkage of the fiber templates, proportional to the exposure time, was also observed (see Figure S1 in the Supporting Information). WO_3 layers of 120

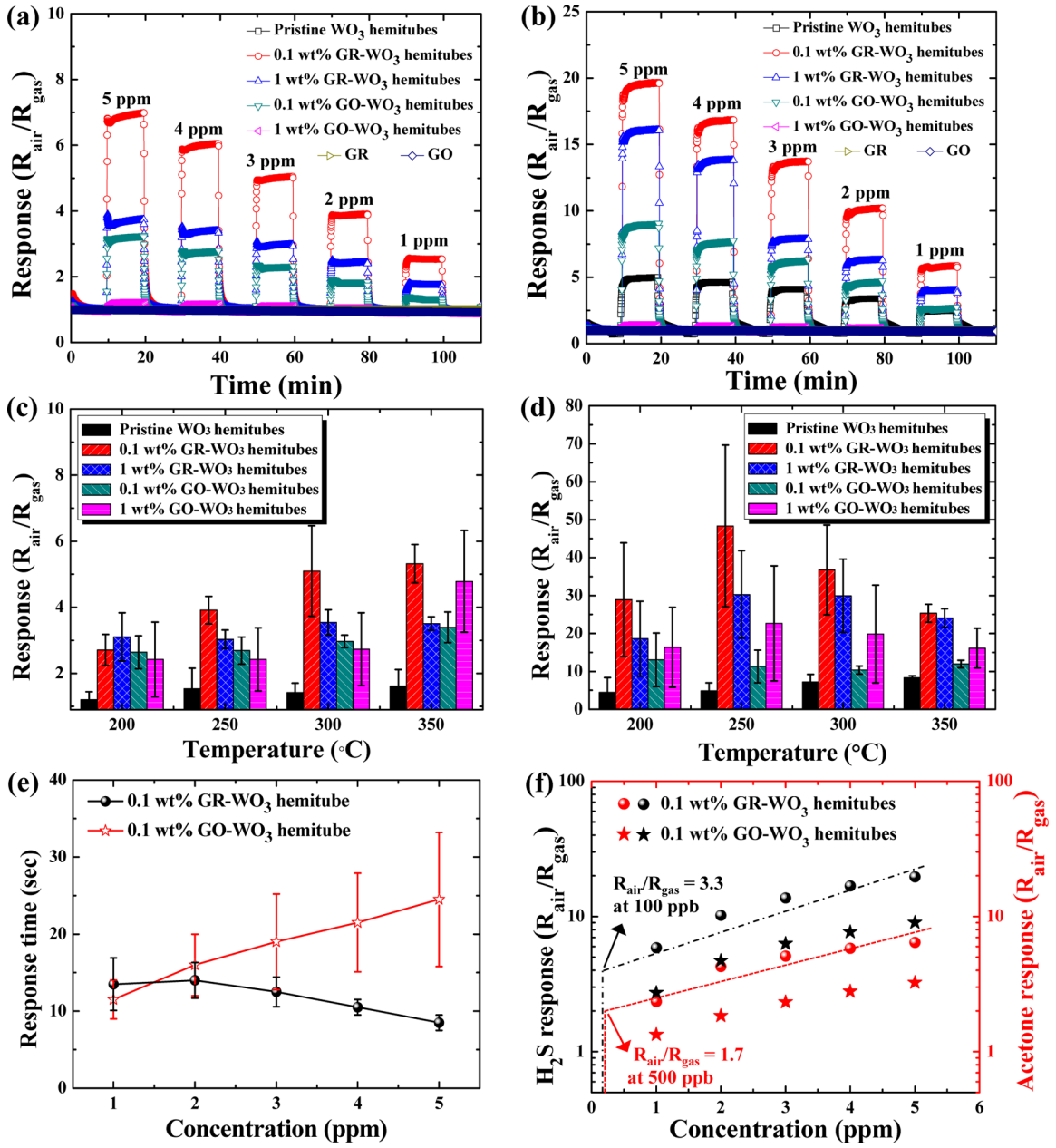

Figure 4. Dynamic sensing characteristics of (a) acetone and (b) H_2S in the gas concentration range of 1−5 ppm at 300 °C in the first cyclic test, response properties toward (c) 5 ppm of acetone and (d) 5 ppm of H_2S in the temperature range of 200−350 °C, (e) response time of 0.1 wt % GR- and 0.1 wt % GO-WO_3 hemitubes in the concentration range of 1−5 ppm at 300 °C toward acetone, (f) limit of detection of 0.1 wt % GR- and 0.1 wt % GO-WO_3 hemitubes toward H_2S and acetone at 300 °C.

nm thickness were coated on the bumpy fiber templates via RF-sputtering. The WO_3 coated fibers retained the rough surface morphology (Figure 2c). High-temperature calcination was subsequently carried out at 500 °C for 1 h to eliminate the core polymer template while crystallizing the thin WO_3 shell layer. This results in bumpy WO_3 shells with open hemitubular structure (Figure 2d) due to the nonconformal deposition behavior of the RF-sputtering method, particularly with respect to the underside of the polymer template.[20,40] The individual hemitubes exhibited diameters of 200−300 nm with wrinkled thin-shell structures (Figure 2e and Figure S3a, b in the Supporting Information). High-resolution TEM analysis revealed that the WO_3 tubes have a highly crystallized monoclinic structure with (002) crystal planes with interplanar distance of 3.84 Å (Figure 2f) at the edge of the hemitube (red dot box). Selected area electron diffraction (SAED) patterns of the WO_3 hemitubes confirm crystallization of the WO_3 structures with characteristic (022) and ($\bar{2}$02) peaks. These correspond to interplanar distances of 2.72 and 2.67 Å, respectively, maintaining an angle of 90° (Figure 2f inset).

Then, the as-synthesized WO_3 hemitubes were functionalized with either very thin graphite (GR) and graphene oxide (GO) by mixing solutions of dispersed WO_3 hemitubes with GR or GO (Figure 2g-l). The obtained solution was then drop coated onto sensor substrates. Images g and h in Figure 2 are scanning electron microscopy (SEM) images of composite layers of the WO_3 hemitubes functionalized with the GR additive (hereafter, GR-WO_3). Folded and stacked graphene layers (white arrows)

dx.doi.org/10.1021/am501394r | ACS Appl. Mater. Interfaces 2014, 6, 9061−9070

can be seen to contact several WO_3 hemitubes at once, resulting in the formation of graphite/WO_3 heterojunctions. GO, which possesses more flexible characteristics (white arrows), is shown well dispersed with WO_3 hemitubes (Figure 2j, k) (hereafter, GO-WO_3). TEM images clearly show that good contact between the hemitubes and the GR and GO layers, respectively (Figure 2i, l and Figure S3c, d in the Supporting Information). In addition, SAED patterns confirmed that the characteristic peaks of GR and GO coexisted with the polycrystalline structure of the WO_3 hemitubes (Inset of Figure 2i and l). Compositional mapping results obtained by energy-dispersive X-ray spectroscopy (EDX) also revealed the homogeneous mixing within the GR-WO_3 and GO-WO_3 layers (Figure S4a−d, e−h in the Supporting Information).

The crystal structures of the GR-WO_3 and GO-WO_3 composites were evaluated using X-ray diffraction (XRD) and compared with those of pure GR and GO layers (see Figure S5 in the Supporting Information). The WO_3 hemitubes showed a single phase monoclinic structure (JCPDS file no. 43−1035). However, in the case of GR-WO_3 (see Figure S5d in the Supporting Information) and GO-WO_3 (Figure S5e in the Supporting Information) composite materials, the characteristic XRD peaks of GR and GO were not observed. This results from the very small amount of GR and GO (0.1 wt %) added to the composites; falling below the detection limits of XRD analysis. To confirm the existence of GR and GO, and their crystal structures, we carried out Raman spectroscopy measurements using a 514 nm laser (see Figure S6 in the Supporting Information). The Raman spectra revealed that the unmodified WO_3 hemitubes (see Figure S6c in the Supporting Information) have a monoclinic crystalline structure[41] and the GO- and GR-WO_3 hemitube composite materials showed clear GO (see Figure S6d in the Supporting Information) and GR (see Figure S6e in the Supporting Information) spectra.

To investigate the nature of the electrical junctions between the GR or GO sheets with the WO_3 hemitubes, we investigated the work functions of the WO_3 hemitubes, GR, and GO by Kelvin probe force microscopy (KPFM) (Figure 3). Figure 3a exhibits the topographic image of a single WO_3 hemitube. Via a cross sectional analysis (Figure 3b), typical dimensions (22 nm height and 139 nm width at bottom) were obtained. The Kelvin contact potential (CPD) image (of the same area as in Figure 3a) is presented in Figure 3c. The CPD is the bias applied between cantilever tip and sample surface in the KPFM mode and equals the difference between the work functions of the tip and sample (Φ_{tip} and Φ_{sample}) divided by the elementary charge e ($V_{CPD} = (\Phi_{tip} - \Phi_{sample})/e$).[42] Figure 3c shows variations in CPD (of some hundred mV) appear with no constant CPD value obtained in the areas surrounding the WO_3 hemitube. Apparently large areas of the HOPG substrate are covered with small fragments of WO_3 hemitubes that bring the effective work function of the substrate toward that of the WO_3 hemitubes, as also seen in the topographic image in Figure 3a. Consequently for this kind of sample, a direct comparison of the work function of the WO_3 hemitube with the one of the underlying HOPG substrate is not possible. In order to determine a reliable work function value for the WO_3 hemitubes, a sample with a very high surface density of WO_3 hemitubes was prepared and compared to a second sample composed of bare HOPG with the well-defined work function of 4.60 ± 0.20 eV.[43−45] To ensure an unchanged work function of the Pt−Ir tip, the cantilever was regularly compared to the bare HOPG reference sample. CPD values on the high coverage WO_3 hemitube sample were taken with two different Pt−Ir cantilever on 60 different locations on the sample surface to obtain the most reliable values. Applying to following expression

$$\Phi_{WO_3 hemitube} = \Phi_{bareHOPG} + e(V_{CPD,bareHOPG} - V_{CPD,WO_3 hemitubes})$$

we obtained a WO_3 hemitube work function of 4.05 ± 0.33 eV. In Figure 3d, the band structure of the WO_3 hemitubes is compared to those of GR and GO in reference to the vacuum energy level. The work function of the hemitubes falls below the values of GR (4.6−4.7 eV)[46] and GO (4.7 eV).[47] Thus, upon contact, electron transfer becomes possible from the WO_3 hemitubes to the GR/GO, resulting in the formation of a depletion layer (Figure 3e). For this Schottky contact, a band-bending value $\Delta E = \Phi_{GR/GO} - \Phi_{WO_3 hemitubes}$ of 0.55 to 0.65 eV can be calculated.

To investigate the VOC sensing characteristics of exhaled breath sensors utilizing pristine WO_3, GO-WO_3, and GR-WO_3 hemitubes, the gas response, detected by examining the change in DC resistance of the bumpy hemitube structure, upon exposure to the gas of interest relative to that in reference air, is used. The sensor response, defined as (R_{air}/R_{gas}) is evaluated at various temperatures in the range of 200−350 °C and in highly humid atmosphere conditions (85−95% RH) as a function of the concentration of biomarker gases such as acetone (CH_3COCH_3) and H_2S, respectively (Figure 4). For an accurate diagnosis of diabetes, a highly sensitive detection of acetone must be achieved in order to distinguish between the relatively small differences in exhaled acetone concentrations, which distinguish healthy humans from those suffering from diabetes, viz., 0.9 and 1.8 ppm, respectively.[2] In the case of diagnosis of halitosis, at least 1 ppm of H_2S should be detected, which is the odor recognizable concentration in the exhaled breath of halitosis patients.[28,48] The VOC sensing results reveal that the 0.1 wt % GR-WO_3 showed the highest response (R_{air}/R_{gas} = 6.96 at 5 ppm) to acetone at 300 °C, a 6.45-fold enhancement relative to that of single phase WO_3 (R_{air}/R_{gas} = 1.08 at 5 ppm), whereas 0.1 wt % GO-WO_3 exhibited a 3-fold higher acetone response (R_{air}/R_{gas} = 3.25 at 5 ppm) (Figure 4a). Functionalization of the WO_3 with GR and GO is therefore demonstrated to lead to major improvements to what is normally a relatively weak response to acetone (R_{air}/R_{gas} = 1.08 at 5 ppm). The acetone response of GR (0.1 wt %)-WO_3 (R_{air}/R_{gas} = 3.9 to 2 ppm at 300 °C) is similar to that (R_{air}/R_{gas} = 4.11 to 2 ppm at 300 °C) of our previous work with Pt-WO_3 hemitubes[20] as well as that (R_{air}/R_{gas} = 3.25 to 1.8 ppm at 400 °C) of 10 mol % Si-doped WO_3 nanoparticles as reported in the literature.[2] Major improvements in sensitivity to H_2S were also obtained by GR and GO functionalization. While unfunctionalized WO_3 showed a sensor response of 4.98 for 5 ppm of H_2S, functionalization with 0.1 wt % GR resulted in a 3.95-fold higher response (R_{air}/R_{gas} = 19.66 at 5 ppm), whereas that with 0.1 wt % GO led to 1.81-fold enhancement (R_{air}/R_{gas} = 9.01 at 5 ppm) (Figure 4b). The improvement in response toward H_2S of GR-WO_3 (R_{air}/R_{gas} = 10.19 to 2 ppm at 300 °C) and GO-WO_3 (R_{air}/R_{gas} = 4.7 to 2 ppm at 300 °C) is remarkably high compared to that (R_{air}/R_{gas} = 1.4 to 2 ppm at 300 °C) of Pt-WO_3 hemitubes reported in our previous work.[20] Larger levels of GR and GO (1 wt %) resulted in reduced enhancement in sensor response to both acetone (R_{air}/R_{gas}= 3.73 for GR and 1.20 for GO at 5 ppm) and H_2S (R_{air}/R_{gas} =

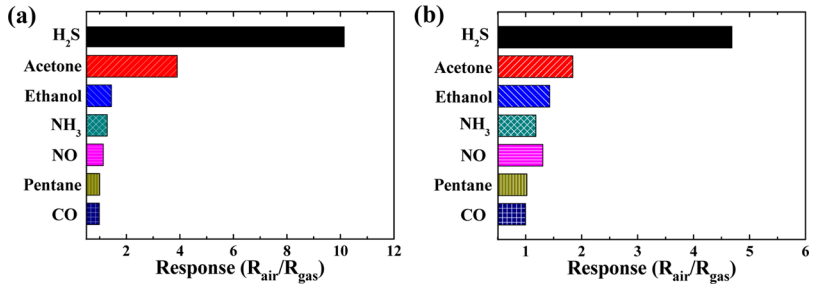

Figure 5. Selective characteristics of: (a) GR (0.1 wt %)-WO_3 and (b) GO (0.1 wt %)-WO_3 with respect to interfering gases (e.g., as CO, C_2H_5OH, NH_3, NO, and C_5H_{12}) at concentrations of 2 ppm.

16.04 for GR and 1.36 for GO at 5 ppm). In order to investigate the role of GR and GO in enhancing gas responses, reference VOC sensors were fabricated, composed solely of pure GR or pure GO layers, which were coated onto two parallel electrodes. The single-phase GR- and GO-based sensors showed no noticeable response to acetone and H_2S gases at 300 °C, while maintaining a constant base resistance of 19.27 kΩ for the GR layers and 187 Ω for the GO layers, respectively (see Figure S7 in the Supporting Information). Surprisingly, the GR modified sensor material exhibited a higher effective resistance than that of the GO modified material, likely a reflection of significant differences in layer thicknesses and morphologies.

Considering the negligible response to acetone and H_2S of pure GR and GO, and the nature of the band bending at the heterojunction structures in Figure 3d, e, GR and GO appear to serve largely as electronic sensitizers within the WO_3 sensing layer. Given the respective work functions, GR and GO should serve to lower the electron concentration, in air, at the surface of the WO_3 hemitubes, which in turn should lead to larger conductivity changes upon exposure to reducing gases.[49−51] Nevertheless, the base resistances of GR-WO_3 (3.16 MΩ at 200 °C) and GO-WO_3 (1.87 MΩ at 200 °C) (see Figure S8 in the Supporting Information) are found to be lower than that of single phase WO_3 (18.99 MΩ at 200 °C), presumably because of the high electrical conductivity through the graphene-based materials, facilitating electron charge carrier transport (see Figure S9 in the Supporting Information).

The temperature dependence and long-term thermal cycling stability of VOC (acetone and H_2S) sensors using GR-WO_3 and GO-WO_3 were characterized following 4 repeated cyclic measurements in the temperature range of 200−350 °C (Figure 4c and d). The results revealed that the response to 5 ppm of acetone of the GR- and GO-WO_3 composites gradually increased with temperature with the maximum response of 5.32 ± 0.58 achieved at 350 °C with 0.1 wt % GR-WO_3 (Figure 4c). For H_2S, maximum response of 48.33 ± 21.32 was obtained upon exposure to 5 ppm of H_2S at 250 °C with 0.1 wt % GR-WO_3 as compared to 4.86 ± 2.13 for the single phase material (Figure 4d).

To investigate the source of the sensor response enhancement, we measured the base resistances of the individual sensors (Figure S8 in the Supporting Information). Interestingly, the resistance of 0.1 wt % GO-WO_3 remained nearly the same regardless of the temperature variation after the first cyclic test (see Figure S8a in the Supporting Information). On the other hand, the resistance of 0.1 wt % GR-WO_3 showed a continuous decrease in base resistance, saturating at approximately 4 MΩ after the third cyclic test (see Figure S8b in the Supporting Information). These different behaviors in base resistance change during repeated cyclic measurements had a great influence on the gas responses as demonstrated in the Supporting Information, Figure S10. Following the morphological investigation of each sensor after the 4 cyclic thermal aging processes, no morphological changes in microstructures of the WO_3 hemitubes were evident. In addition, the presence of GR and GO was confirmed using SEM imaging after four cyclic thermal aging processes (see Figure S11 in the Supporting Information). Thus, some preaging steps (2 or 3 cyclic measurements) appear to provide much enhanced sensing stability over broad ranges of operating temperature.

To further confirm the suitability of 0.1 wt % GR- and GO-WO_3 hemitubes as exhaled breath sensors for real time diagnosis of diabetes and halitosis, we evaluated the response (τ_{res}) and recovery times (τ_{recov}) toward acetone and H_2S in the ranges of 1−5 ppm at 300 °C (Figure 4e and Figure S12−S13 in the Supporting Information). Considering the duration of human exhaled breath, the response time should be under 15 s for practical applications. The 0.1 wt % GR-WO_3 sensor was found to show rapid response (13.5 ± 3.4 s at 1 ppm acetone) with the response time shortened to 8.5 ± 1.0 s as the acetone concentration increased to 5 ppm. In contrast, 0.1 wt % GO-WO_3 showed a response time of 11.5 ± 2.5 s for 1 ppm of acetone with an increase to 24.5 ± 8.7 s for 5 ppm acetone. Very fast response (<15 s) and recovery (<30 s) times were achieved compared to those (τ_{res} and τ_{recov} ≈ 300 s) of Pt-WO_3 hemitubes reported in our previous work.[20] The faster responding and recovery speeds of GR- and GO-WO_3 than that of pristine WO_3 are attributed, as discussed above, to the overall decrease in the circuit RC time constant, the former factor related to the much higher conductivity of GR-WO_3 and GO-WO_3 composites vs single phase WO_3 and reduced interfacial capacitance related to the ready injection of charge carriers from WO_3 to GR/GO (see Figure S14 in the Supporting Information).

To investigate the source of variation in base resistance and reaction/recovery kinetics, we performed Raman spectroscopy measurements on samples obtained after the forth cycle test (see Figure S15 in the Supporting Information). Severe destruction of sp^2 bonding and the generation of defects in GO and GR were identified. Considering variations in the base resistances and response/recovery times, GO-WO_3 showed more stable sensing characteristics compared to GR-WO_3 presumably due to the higher thermal stability of graphene oxide compared to graphene in air atmosphere at elevated sensing temperatures (200−350 °C). Long-term sensing stability was also examined with the finding that there was less variation in response toward acetone and H_2S with GO-WO_3 as compared to that of GR-WO_3 (see Figure S16 in the Supporting Information). The variations in response were

mainly attributed to base resistance changes in the range of 22−25% following 9 months cyclic thermal aging (see Figure S17 in the Supporting Information). Note that the cyclic thermal aging was performed at least 10 times at 300 °C for 9 months. The limit of detection (LOD) toward H_2S and acetone was estimated using linear extrapolation. The results show that 0.1 wt % GR-WO_3 can detect down to 100 ppb (R_{air}/R_{gas} = 1.7 for acetone and R_{air}/R_{gas} = 3.3 for H_2S), considerably lower than the exhaled acetone concentration of a healthy human (~900 ppb) and the exhaled H_2S for recognizable concentrations representative of halitosis (1 ppm) (Figure 4f). The selective properties were evaluated to verify that the proposed GR (0.1 wt %)-WO_3 and GO (0.1 wt %)-WO_3 hemitube sensors exhibited highly H_2S as well as acetone selective characteristics with respect to interfering gases at 2 ppm in highly humid ambient (85−95% RH) (i.e., CO, C_2H_5OH, NH_3, NO, and C_5H_{12}), which are known biomarkers in exhaled breath (Figure 5). The H_2S and acetone selective sensing properties can be utilized for the diagnosis of diabetes and halitosis by pattern recognition applied to exhaled breath.[52,53]

CONCLUSIONS

In summary, we investigated the VOCs sensing properties of bumpy, high-surface-area WO_3 hemitubes, functionalized by either thin graphite or graphene oxide layers for the diagnosis of diabetes and halitosis. The WO_3 hemitubes were prepared via O_2 plasma treatment of electrospun fiber templates onto which WO_3 films were RF-sputtering, followed by high temperature calcination. A remarkable enhancement in VOC sensing response was achieved upon further functionalization with GR and GO. In particular, 0.1 wt % GR functionalized WO_3 hemitubes showed a superior response (6.45-fold for 5 ppm acetone and 3.95-fold for 5 ppm of H_2S at 300 °C) compared to single phase WO_3 hemitubes. A minimum detectable concentration of 100 ppb was estimated with 0.1 wt % GR-WO_3, low enough to analyze the exhaled acetone and H_2S for the diagnosis of diseases. In addition, fast response (<15 s) and recovery (<30 s) of 0.1 wt % GR- and 0.1 wt % GO-WO_3 toward acetone and H_2S demonstrated excellent potential for real-time exhaled breath diagnosis of diabetes and halitosis. Furthermore, the effect of cyclic thermal aging on the sensing behavior and the response/recovery time characteristics of composites based on WO_3 hemitubes and graphene have been investigated for the first time. The GO-WO_3 showed a steady state resistance approximately independent of sensing temperatures. In contrast, GR-WO_3 showed a gradual saturation of sensor resistance saturation with a minimal temperature dependence, which resulted in significant changes in response and reaction/recovery times. On the basis of these results, we conclude that the control of the amount of graphene based additives, and the thermal aging step, has a crucial impact on the sensing characteristics of composite materials and will provide new sensing materials for the application in diabetes and halitosis diagnosis by exhaled breath analysis.

ASSOCIATED CONTENT

Supporting Information

Morphological changes of PVP/PMMA composite fibers during the oxygen plasma treatment with different treatment times, additional TEM observation of WO_3 hemitube, EDX elemental mapping of GR-WO_3 hemitube and GO-WO_3 hemitube, XRD analysis, Raman spectroscopy analysis, gas sensing properties of pristine GR and GO, base resistance changes of GR-WO_3 hemitube and GO-WO_3 hemitube under the 4-cyclic thermal aging, base resistance of pristine WO_3 hemitube, gas response of behavior during cyclic thermal aging of GR-WO_3 hemitube and GO-WO_3 hemitube, SEM observation of GR-WO_3 hemitube and GO-WO_3 hemitube after cyclic thermal aging test, response and recovery times, capacitance and resistance at different frequency range to confirm RC time delay, Raman spectroscopy analysis after cyclic thermal aging, schematic setup for the gas sensing and optical images of sensor substrate, sensing stability following 9 month cyclic thermal aging. This material is available free of charge via the Internet at http://pubs.acs.org.

AUTHOR INFORMATION

Corresponding Author

*E-mail: idkim@kaist.ac.kr.

Notes

The authors declare no competing financial interest.

ACKNOWLEDGMENTS

This work was supported by the Center for Integrated Smart Sensors funded by the Ministry of Science, ICT & Future Planning as Global Frontier Project (CISS- 2011-0031870).

REFERENCES

(1) Shin, J.; Choi, S. J.; Youn, D. Y.; Kim, I. D. Exhaled VOCs Sensing Properties of WO_3 Nanofibers Functionalized by Pt and IrO_2 Nanoparticles for Diagnosis of Diabetes and Halitosis. *J. Electroceram.* **2012**, *29*, 106−116.

(2) Righettoni, M.; Tricoli, A.; Pratsinis, S. E. Si:WO_3 Sensors for Highly Selective Detection of Acetone for Easy Diagnosis of Diabetes by Breath Analysis. *Anal. Chem.* **2010**, *82*, 3581−3587.

(3) Awano, S.; Ansai, T.; Takata, Y.; Soh, I.; Yoshida, A.; Hamasaki, T.; Kagiyama, S.; Nakamichi, I.; Sonoki, K.; Takehara, T. Relationship between Volatile Sulfur Compounds in Mouth Air and Systemic Disease. *J. Breath Res.* **2008**, *2*, 017012.

(4) Narasimhan, L. R.; Goodman, W.; Patel, C. K. N. Correlation of Breath Ammonia with Bood Urea Nitrogen and Creatinine During Hemodialysis. *Proc. Natl. Acad. Sci. U.S.A.* **2001**, *98*, 4617−4621.

(5) Tseliou, E.; Bessa, V.; Hillas, G.; Delimpoura, V.; Papadaki, G.; Roussos, C.; Papiris, S.; Bakakos, P.; Loukides, S. Exhaled Nitric Oxide and Exhaled Breath Condensate pH in Severe Refractory Asthma. *Chest* **2010**, *138*, 107−113.

(6) Peng, G.; Tisch, U.; Adams, O.; Hakim, M.; Shehada, N.; Broza, Y. Y.; Billan, S.; Abdah-Bortnyak, R.; Kuten, A.; Haick, H. Diagnosing Lung Cancer in Exhaled Breath Using Gold Nanoparticles. *Nat. Nanotechnol.* **2009**, *4*, 669−673.

(7) Phillips, M.; Gleeson, K.; Hughes, J. M. B.; Greenberg, J.; Cataneo, R. N.; Baker, L.; McVay, W. P. Volatile Organic Compounds in Breath as Markers of Lung Cancer: A Cross-Sectional Study. *Lancet* **1999**, *353*, 1930−1933.

(8) Oneill, H. J.; Gordon, S. M.; Oneill, M. H.; Gibbons, R. D.; Szidon, J. P. A Computerized Classification Technique for Screening for the Presence of Breath Biomarkers in Lung-Cancer. *Clin. Chem.* **1988**, *34*, 1613−1618.

(9) Kamat, P. C.; Roller, C. B.; Namjou, K.; Jeffers, J. D.; Faramarzalian, A.; Salas, R.; McCann, P. J. Measurement of Acetaldehyde in Exhaled Breath Using a Laser Absorption Spectrometer. *Appl. Opt.* **2007**, *46*, 3969−3975.

(10) Lord, H.; Yu, Y. F.; Segal, A.; Pawliszyn, J. Breath Analysis and Monitoring by Membrane Extraction with Sorbent Interface. *Anal. Chem.* **2002**, *74*, 5650−5657.

(11) Kim, I. D.; Rothschild, A.; Tuller, H. L. Advances and New Directions in Gas-Sensing Devices. *Acta Mater.* **2013**, *61*, 974−1000.

(12) Kim, H. J.; Choi, K. I.; Pan, A. Q.; Kim, I. D.; Kim, H. R.; Kim, K. M.; Na, C. W.; Cao, G. Z.; Lee, J. H. Template-Free Solvothermal

Synthesis of Hollow Hematite Spheres and their Applications in Gas Sensors and Li-ion Batteries. *J. Mater. Chem.* **2011**, *21*, 6549−6555.
(13) Choi, S. H.; Hwang, I. S.; Lee, J. H.; Oh, S. G.; Kim, I. D. Microstructural Control and Selective C_2H_5OH Sensing Properties of Zn_2SnO_4 Nanofibers Prepared by Electrospinning. *Chem. Commun.* **2011**, *47*, 9315−9317.
(14) Nguyen, H.; El-Safty, S. A. Meso- and Macroporous Co_3O_4 Nanorods for Effective VOC Gas Sensors. *J. Phys. Chem. C* **2011**, *115*, 8466−8474.
(15) Breedon, M.; Spizzirri, P.; Taylor, M.; du Plessis, J.; McCulloch, D.; Zhu, J. M.; Yu, L. S.; Hu, Z.; Rix, C.; Wlodarski, W.; Kalantar-Zadeh, K. Synthesis of Nanostructured Tungsten Oxide Thin Films: A Simple, Controllable, Inexpensive, Aqueous Sol-Gel Method. *Cryst. Growth Des.* **2010**, *10*, 430−439.
(16) Zheng, H. D.; Ou, J. Z.; Strano, M. S.; Kaner, R. B.; Mitchell, A.; Kalantar-Zadeh, K. Nanostructured Tungsten Oxide - Properties, Synthesis, and Applications. *Adv. Funct. Mater.* **2011**, *21*, 2175−2196.
(17) Penza, M.; Tagliente, M. A.; Mirenghi, L.; Gerardi, C.; Martucci, C.; Cassano, G. Tungsten Trioxide (WO_3) Sputtered Thin Films for a NO_x Gas Sensor. *Sens. Actuators, B* **1998**, *50*, 9−18.
(18) Zhang, Y.; Li, J. P.; An, G. M.; He, X. L. Highly Porous SnO_2 Fibers by Electrospinning and Oxygen Plasma Etching and its Ethanol-Sensing Properties. *Sens. Actuators, B* **2010**, *144*, 43−48.
(19) Shin, J.; Choi, S. J.; Lee, I.; Youn, D. Y.; Park, C. O.; Lee, J. H.; Tuller, H. L.; Kim, I. D. Thin-Wall Assembled SnO_2 Fibers Functionalized by Catalytic Pt Nanoparticles and their Superior Exhaled-Breath-Sensing Properties for the Diagnosis of Diabetes. *Adv. Funct. Mater.* **2013**, *23*, 2357−2367.
(20) Choi, S. J.; Lee, I.; Jang, B. H.; Youn, D. Y.; Ryu, W. H.; Park, C. O.; Kim, I. D. Selective Diagnosis of Diabetes Using Pt-Functionalized WO_3 Hemitube Networks As a Sensing Layer of Acetone in Exhaled Breath. *Anal. Chem.* **2013**, *85*, 1792−1796.
(21) Toyooka, T.; Hiyama, S.; Yamada, Y. A Prototype Portable Breath Acetone Analyzer for Monitoring Fat Loss. *J. Breath Res.* **2013**, *7*, 036005.
(22) Kim, S. J.; Hwang, I. S.; Na, C. W.; Kim, I. D.; Kang, Y. C.; Lee, J. H. Ultrasensitive and Selective C_2H_5OH Sensors Using Rh-Loaded In_2O_3 Hollow Spheres. *J. Mater. Chem.* **2011**, *21*, 18560−18567.
(23) Hwang, I. S.; Choi, J. K.; Woo, H. S.; Kim, S. J.; Jung, S. Y.; Seong, T. Y.; Kim, I. D.; Lee, J. H. Facile Control of C_2H_5OH Sensing Characteristics by Decorating Discrete Ag Nanoclusters on SnO_2 Nanowire Networks. *ACS Appl. Mater. Interfaces* **2011**, *3*, 3140−3145.
(24) Yang, D. J.; Kamienchick, I.; Youn, D. Y.; Rothschild, A.; Kim, I. D. Ultrasensitive and Highly Selective Gas Sensors Based on Electrospun SnO_2 Nanofibers Modified by Pd Loading. *Adv. Funct. Mater.* **2010**, *20*, 4258−4264.
(25) Righettoni, M.; Tricoli, A.; Gass, S.; Schmid, A.; Amann, A.; Pratsinis, S. E. Breath Acetone Monitoring by Portable Si:WO_3 Gas Sensors. *Anal. Chim. Acta* **2012**, *738*, 69−75.
(26) Righettoni, M.; Schmid, A.; Amann, A.; Pratsinis, S. E. Correlations between Blood Glucose and Breath Components from Portable Gas Sensors and PTR-TOF-MS. *J. Breath Res.* **2013**, *7*, 037110.
(27) Salehi-Khojin, A.; Estrada, D.; Lin, K. Y.; Bae, M. H.; Xiong, F.; Pop, E.; Masel, R. I. Polycrystalline Graphene Ribbons as Chemiresistors. *Adv. Mater.* **2012**, *24*, 53−57.
(28) Choi, S. J.; Jang, B. H.; Lee, S. J.; Min, B. K.; Rothschild, A.; Kim, I. D. Selective Detection of Acetone and Hydrogen Sulfide for the Diagnosis of Diabetes and Halitosis Using SnO_2 Nanofibers Functionalized with Reduced Graphene Oxide Nanosheets. *ACS Appl. Mater. Interfaces* **2014**, *6*, 2588−2597.
(29) Lu, G. H.; Ocola, L. E.; Chen, J. H. Room-Temperature Gas Sensing Based on Electron Transfer between Discrete Tin Oxide Nanocrystals and Multiwalled Carbon Nanotubes. *Adv. Mater.* **2009**, *21*, 2487−2491.
(30) Johnson, J. L.; Behnam, A.; Pearton, S. J.; Ural, A. Hydrogen Sensing Using Pd-Functionalized Multi-Layer Graphene Nanoribbon Networks. *Adv. Mater.* **2010**, *22*, 4877−4480.
(31) Basu, S.; Bhattacharyya, P. Recent Developments on Graphene and Graphene oxide Based Solid State Gas Sensors. *Sens. Actuators, B* **2012**, *173*, 1−21.
(32) Yuan, W. J.; Liu, A. R.; Huang, L.; Li, C.; Shi, G. Q. High-Performance NO_2 Sensors Based on Chemically Modified Graphene. *Adv. Mater.* **2013**, *25*, 766−771.
(33) Srivastava, S.; Jain, K.; Singh, V. N.; Singh, S.; Vijayan, N.; Dilawar, N.; Gupta, G.; Senguttuvan, T. D. Faster Response of NO_2 Sensing in Graphene-WO_3 Nanocomposites. *Nanotechnology* **2012**, *23*, 205501.
(34) Zhang, Z. Y.; Zou, R. J.; Song, G. S.; Yu, L.; Chen, Z. G.; Hu, J. Q. Highly Aligned SnO_2 Nanorods on Graphene Sheets for Gas Sensors. *J. Mater. Chem.* **2011**, *21*, 17360−17365.
(35) Singh, G.; Choudhary, A.; Haranath, D.; Joshi, A. G.; Singh, N.; Singh, S.; Pasricha, R. ZnO Decorated Luminescent Graphene as a Potential Gas Sensor at Room Temperature. *Carbon* **2012**, *50*, 385−394.
(36) Hummers, W. S., Jr; Offeman, R. E. Preparation of Graphitic Oxide. *J. Am. Chem. Soc.* **1958**, *80*, 1339.
(37) Spadafora, E. J.; Saint-Aubin, K.; Celle, C.; Demadrille, R.; Grevin, B.; Simonato, J. P. Work Function Tuning for Flexible Transparent Electrodes Based on Functionalized Metallic Single Walled Carbon Nanotubes. *Carbon* **2012**, *50*, 3459−3464.
(38) Choi, S. H.; Ankonina, G.; Youn, D. Y.; Oh, S. G.; Hong, J. M.; Rothschild, A.; Kim, I. D. Hollow ZnO Nanofibers Fabricated Using Electrospun Polymer Templates and Their Electronic Transport Properties. *ACS Nano* **2009**, *3*, 2623−2631.
(39) Cvelbar, U.; Pejovnik, S.; Mozetie, M.; Zalar, A. Increased Surface Roughness by Oxygen Plasma Treatment of Graphite/Polymer Composite. *Appl. Surf. Sci.* **2003**, *210*, 255−261.
(40) Cho, N. G.; Kim, I. D. NO_2 Gas Sensing Properties of Amorphous $InGaZnO_4$ Submicron-Tubes Prepared by Polymeric Fiber Templating Route. *Sens. Actuators, B* **2011**, *160*, 499−504.
(41) Santato, C.; Odziemkowski, M.; Ulmann, M.; Augustynski, J. Crystallographically Oriented Mesoporous WO_3 Films: Synthesis, Characterization, and Applications. *J. Am. Chem. Soc.* **2001**, *123*, 10639−10649.
(42) Melitz, W.; Shen, J.; Kummel, A. C.; Lee, S. Kelvin Probe Force Microscopy and its Application. *Surf. Sci. Rep.* **2011**, *66*, 1−27.
(43) Palma, M.; Levin, J.; Lemaur, V.; Liscio, A.; Palermo, V.; Cornil, J.; Geerts, Y.; Lehmann, M.; Samori, P. Self-Organization and Nanoscale Electronic Properties of Azatriphenylene-Based Architectures: A Scanning Probe Microscopy Study. *Adv. Mater.* **2006**, *18*, 3313−3317.
(44) Beerbom, M. M.; Lagel, B.; Cascio, A. J.; Doran, B. V.; Schlaf, R. Direct Comparison of Photoemission Spectroscopy and in situ Kelvin Probe Work Function Measurements on Indium Tin Oxide Films. *J. Electron Spectrosc. Relat. Phenom.* **2006**, *152*, 12−17.
(45) Liu, P.; Wei, Y.; Jiang, K. L.; Sun, Q.; Zhang, X. B.; Fan, S. S.; Zhang, S. F.; Ning, C. G.; Deng, J. K. Thermionic Emission and Work Function of Multiwalled Carbon Nanotube Yarns. *Phys. Rev. B* **2006**, *73*, 235412.
(46) Suzuki, S.; Bower, C.; Watanabe, Y.; Zhou, O. Work Functions and Valence Band States of Pristine and Cs-Intercalated Single-Walled Carbon Nanotube Bundles. *Appl. Phys. Lett.* **2000**, *76*, 4007−4009.
(47) Liu, J.; Xue, Y. H.; Gao, Y. X.; Yu, D. S.; Durstock, M.; Dai, L. M. Hole and Electron Extraction Layers Based on Graphene Oxide Derivatives for High-Performance Bulk Heterojunction Solar Cells. *Adv. Mater.* **2012**, *24*, 2228−2233.
(48) Tangerman, A.; Winkel, E. G. Extra-Oral Halitosis: An Overview. *J. Breath Res.* **2010**, *4*, 017003.
(49) Yamazoe, N.; Shimanoe, K. New Perspectives of Gas Sensor Technology. *Sens. Actuators, B* **2009**, *138*, 100−107.
(50) Kugishima, M.; Shimanoe, K.; Yamazoe, N. C_2H_4O Sensing Properties for Thick Film Sensor Using La_2O_3-Modified SnO_2. *Sens. Actuators, B* **2006**, *118*, 171−176.
(51) Russo, P. A.; Donato, N.; Leonardi, S. G.; Baek, S.; Conte, D. E.; Neri, G.; Pinna, N. Room-Temperature Hydrogen Sensing with

Heteronanostructures Based on Reduced Graphene Oxide and Tin Oxide. *Angew. Chem., Int. Ed.* **2012**, *51*, 11053−11057.
(52) Tyszkiewicz, C.; Szpakowski, A.; Pustelny, T. Gas Sensing Supported by Pattern Recognition. *Acta Phys. Polym., A* **2009**, *116*, 419−421.
(53) Kim, E.; Lee, S.; Kim, J. H.; Kim, C.; Byun, Y. T.; Kim, H. S.; Lee, T. Pattern Recognition for Selective Odor Detection with Gas Sensor Arrays. *Sensors* **2012**, *12*, 16262−16273.